İSTANBUL UNIVERSITY
CERRAHPAŞA

ORIGINAL ARTICLE
Electrica 2021; 21(3): 468-479

Non-Imaging Permittivity and Temperature Change Detection by Coherent Microwave Radiometry

Cüneyt Utku, Onur Arı

Informatics and Information Security Research Center, Scientific and Technological Research Council of Turkey (Tubitak Bilgem), Kocaeli, Turkey

Cite this article as: C. Utku and O. Ari. "Non-imaging Permittivity and Temperature Change Detection by Coherent Microwave Radiometry," *Electrica*, vol. 21, no. 3, pp. 468-479, Sep. 2021.

ABSTRACT

A non-imaging change (anomaly) detection technique using coherent microwave radiometry is reported. The technique is based on the partial coherence that exists in thermal electromagnetic fields radiated by lossy dielectric objects. The underlying physics permits detection of change in both temperature and permittivity of the object. The statistical approach uses partial coherence measurements of the thermal radiation to derive a statistic which is subsequently used in a generalized likelihood ratio test to determine the presence of change. Monte-Carlo simulations show that the proposed technique can be effective in detection of small anomalies that are challenging to be resolved by other microwave imaging techniques. Detection performance largely depends on the sensitivity and the signal-to-noise ratio of the radiometric system.

***Index Terms*—**Change detection, coherence, correlation radiometry, interferometric radiometry, microwave radiometry, microwave thermography

I. INTRODUCTION

Detection of temperature and permittivity change by non-destructive testing (NDT) is an area of active research in the microwave (MW) community. In the medical domain, specifically in detection of cancer, change is associated with both temperature and permittivity, leading to two main modalities in tumor detection. Active MW modalities take advantage of the permittivity contrast between tumor and healthy background tissue (i) in quantitative imaging where the permittivity profile of the tissue is reconstructed by mathematical inversion of the governing equations of the scattering process or (ii) in radar-based qualitative imaging where a representation of contrasts in scattering potential is constructed and mathematical inversion for permittivity reconstruction is avoided. An extensive list of references for active imaging methods can be found in [1–3]. On the other hand, passive MW modalities, collectively referred to as MW thermography, aim to image the temperature distribution inside the tissue to detect tumors by observing the rise in temperature due to increased metabolic activity induced by tumor growth [4,5].

Recently, the Microwave Radiometric Coherence Imaging (MRCI) technique was proposed for permittivity reconstruction that is based on the partial coherence (cross correlations) of thermal electromagnetic (EM) fields radiated by an object and measured at a discrete set of points [6]. Both MW thermography and MRCI share the same physical fundamentals involving EM theory and the thermal state of the object of interest. In fact, the autocorrelation of the thermal EM fields at each point (a subset of the cross correlations) is precisely the intensity of thermal radiation, which is the fundamental quantity of interest in MW thermography. Thus, in principle, MRCI offers a means for the simultaneous reconstruction of permittivity and temperature; a premise yet to be demonstrated. The use of partial cross-correlations of thermal EM fields for formation of high-resolution brightness temperature images, known as aperture synthesis in interferometric radiometry (SAIR), has a long history in radio astronomy [7]. Aperture synthesis was later also adopted in passive remote sensing [8]. Similar in principle, correlation radiometry was proposed as a means in thermography for high-resolution quantitative imaging of

Corresponding Author:
Cüneyt Utku

E-mail: cuneyt.utku@tubitak.gov.tr

Received: May 19, 2021

Accepted: July 29, 2021

DOI: 10.5152/electr.2021.21050

temperature distribution within a volume [9]. In the far-field, under nonrestrictive conditions, SAIR was also shown to be related to MRCI in [6]. Among several areas for future research, the possibility of a qualitative extension to the MRCI technique was also pointed out. In this follow-up study, such a qualitative non-imaging technique is proposed for the detection of permittivity/temperature change (anomaly) in an object with finite conductivity, thus extending the applications of MW radiometric coherence data to potential new areas beyond those currently available with SAIR. In order to distinguish it from MRCI, the current non-imaging study will be referred to the as coherent microwave radiometry (CMR). The obvious advantage of the CMR technique is that it provides a fast means for change detection with far less demand for hardware and computational resources than a MW imaging system. Moreover, quantitative MW imaging involves an inverse problem associated with image formation which is generally ill-posed and the reconstructed images are of low resolution. Non-imaging detection, on the other hand, is always well-posed, and the size of the smallest detectable anomaly is predominantly determined by the signal-to-noise ratio (SNR) (defined for radiometric systems) or the noise-equivalent differential temperature (sensitivity) of the radiometric system. The current method employs composite hypothesis testing using the Generalized Likelihood Ratio Test (GLRT) [10]. In SAIR, Trott et al. [11] have used GLRT with interferometric visibility data for detection of transient astronomical sources. GLRT has also been proposed for detection of buried objects with ground-penetrating radar [12], detection of breast cancer in radar imaging [13], and detection of objects in time-reversal imaging [14,15]. Although the current study is based on GLRT with CMR data, its use is merely to demonstrate the potential of CMR to infer permittivity/ temperature change from the measured cross-correlations of thermal EM fields. Similar results may also be obtained using alternative methods with CMR data.

The paper is organized as follows. In the next section, a summary of the fundamental quantities and equations in CMR is discussed. Incorporation of cross-correlation measurements into the GLRT framework is also shown here. The following section on numerical simulations explores various aspects of the detection performance through the use of Monte-Carlo simulations and analysis of the Receiver Operating Characteristics (ROC) corresponding to different detection scenarios. The following section briefly discusses some current issues and drawbacks related to the proposed method. We finalize with a conclusion section.

Notation: Lower-case bold letters may denote (i) a physical vector quantity like the position vector $\boldsymbol{r}$, (ii) a tuple like $\boldsymbol{\psi} = (\theta,\phi)$ or (iii) a real-valued column vector of arbitrary length (e.g. a data vector $\boldsymbol{x}$). The superscript 'T' denotes the transpose and vectors with subscripts are used to denote either an electric field corresponding to a specific polarization of the source current inducing the field (e.g. $\boldsymbol{E}_p$ and $\boldsymbol{e}_p$) or a data vector corresponding to a specific measurement (e.g. the data vector $\boldsymbol{x}_m$ corresponding to the m'th measurement). Upper-case Greek letters in bold denote matrices (e.g. $\boldsymbol{\Gamma}$ and $\boldsymbol{\Lambda}$). Finally, $\boldsymbol{x} \sim \mathcal{N}(\boldsymbol{\kappa},\boldsymbol{\Lambda})$ indicates that the random data vector $\boldsymbol{x}$ is normally distributed with mean vector $\boldsymbol{\kappa}$ and covariance matrix $\boldsymbol{\Lambda}$.

II. COHERENT MICROWAVE RADIOMETRY FOR CHANGE DETECTION

The mutual-intensity matrix (mutual coherence for simultaneous EM field measurements) contains information on the temperature distribution, electrical properties, and structure of the object under investigation. Referring to Fig. 1, where there is an object in free space with relative permittivity $\varepsilon_r(\boldsymbol{r})$, conductivity $\sigma(\boldsymbol{r})$ and temperature $T(\boldsymbol{r})$ (all functions of position $\boldsymbol{r}$), the co-polarized mutual intensity of thermal MW

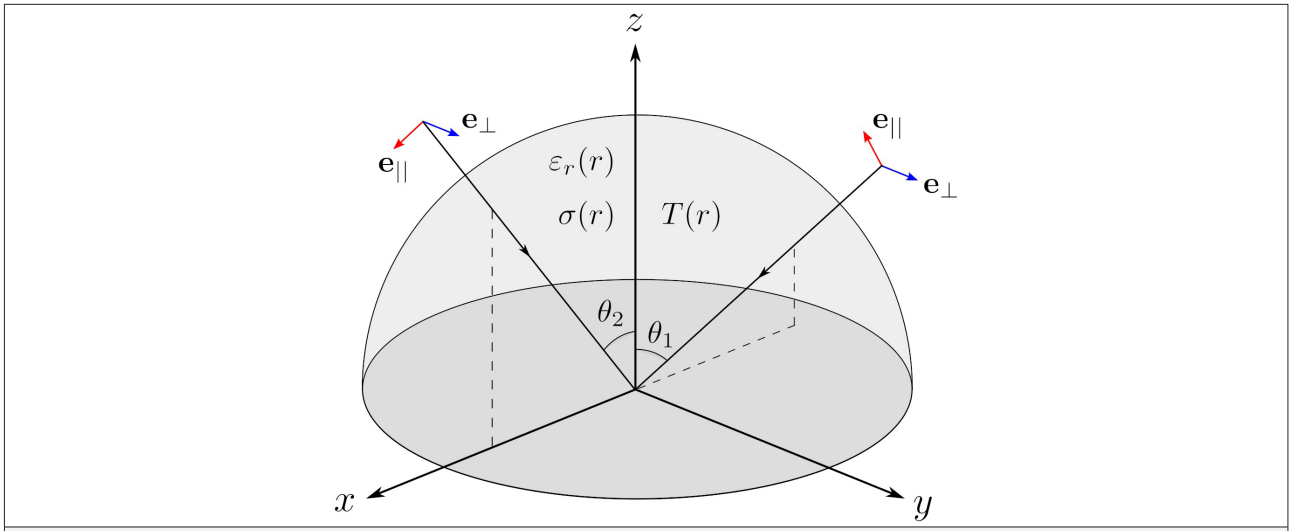

Fig. 1. Coherent observation of the thermal EM fields emitted by a hemispherical lossy dielectric object. Parallel and perpendicular polarization unit vectors are denoted by $e_{\parallel}$ and $e_{\perp}$ respectively.

radiation observed at points $\boldsymbol{r}_1$ and $\boldsymbol{r}_2$ external to the object is given by [6]

$$\Gamma_p(\boldsymbol{r}_1,\boldsymbol{r}_2)=\frac{4k_B k_o^3\eta_o B}{\pi}\int_{V_H} T(\boldsymbol{r}')\sigma(\boldsymbol{r}')\boldsymbol{E}_p(\boldsymbol{r}',\boldsymbol{r}_1)\cdot\boldsymbol{E}_p^*(\boldsymbol{r}',\boldsymbol{r}_2)dv' \qquad (1)$$

where V_H is the volume subtended by the object, k_B is Boltzmann's constant, k_o is the wave number in free space, η_o is characteristic impedance of free space, and B is the radiometer receiver bandwidth. Furthermore, p denotes the polarization state of the co-polarized mutual intensity and $\boldsymbol{E}_p(\boldsymbol{r}',\boldsymbol{r})$ is the electric field induced at $\boldsymbol{r}'$, inside the object, by a p-polarized point source located at the observation point $\boldsymbol{r}$. In (1), it is inherently assumed that the effect of external (to the object) blackbody radiation has been eliminated. In the far field of the object, the internal electric field of the object has the form

$$\boldsymbol{E}_p(\boldsymbol{r}',\boldsymbol{r})\approx\frac{e^{ikr}}{4\pi r}\boldsymbol{e}_p(\boldsymbol{r}',\boldsymbol{\psi}) \qquad (2)$$

where $\boldsymbol{\psi}=(\theta,\phi)$ is a short-hand notation, with θ and ϕ being the polar and azimuth angles of point $\boldsymbol{r}$, respectively. The polarization state, in this case, is conveniently defined by the parallel and perpendicular vectors to the plane of incidence, that is, plane of constant ϕ. The unit polarization vectors are shown as the red and blue vectors for parallel and perpendicular polarizations, respectively. With this far-field expression and normalization by the factor $k_B k_o^3\eta_o B/4\pi^3 r^2$, equation (1) reduces to the simpler form:

$$\Gamma_p^{(N)}(\boldsymbol{\psi}_1,\boldsymbol{\psi}_2)=\int_{V_H} T(\boldsymbol{r}')\sigma(\boldsymbol{r}')\boldsymbol{e}_p(\boldsymbol{r}',\boldsymbol{\psi}_1)\cdot\boldsymbol{e}_p^*(\boldsymbol{r}',\boldsymbol{\psi}_2)dv' \qquad (3)$$

where the superscript '(N)' denotes normalization. This expression will later be evaluated for various pairs of $\boldsymbol{\psi}_1$ and $\boldsymbol{\psi}_2$ using the following simple quadrature for the volume integration using small cubic cells having volume Δv as:

$$\Gamma_p^{(N)}(\boldsymbol{\psi}_1,\boldsymbol{\psi}_2)\approx\Delta v\sum_{j=1}^{N_H} T(\boldsymbol{r}_j)\sigma(\boldsymbol{r}_j)\sum_{q\in\{x,y,z\}} e_{qp}(\boldsymbol{r}_j,\boldsymbol{\psi}_1)e_{qp}^*(\boldsymbol{r}_j,\boldsymbol{\psi}_2) \qquad (4)$$

The inner sum in (4) corresponds to the dot product of the field vectors represented with Cartesian components $e_{qp},(q\in\{x,y,z,\})$ of the vector $\boldsymbol{e}_p$. A measurement of complex-valued mutual intensity is made by time-correlating the fields observed at the field points $\boldsymbol{r}_i$ and $\boldsymbol{r}_j$. Specifically, for the pair $(\boldsymbol{r}_i,\boldsymbol{r}_i)$ the time cross-correlation Γ_{ij}, is defined through its real and imaginary parts as

$$\mathcal{R}e\{\Gamma_{ij}\}=2\overline{\mathcal{E}_i^{(R)}(t)\mathcal{E}_j^{(R)}(t)} \qquad (5)$$

$$\mathcal{I}m\{\Gamma_{ij}\}=2\overline{\mathcal{E}_i^{(R)}(t)\mathcal{E}_j^{(I)}(t)}, \qquad (6)$$

respectively, where the overbar denotes time-averaging and the quantities $\mathcal{E}_i^{(R)}(t)$ and $\mathcal{E}_i^{(I)}(t)$ are the real and imaginary parts of the analytic signal representation of the field observed at $\boldsymbol{r}_i$. The measurement equation for mutual intensity is then given by

$$\Gamma_{ij}=\Gamma_p^{(N)}(\theta_i,\theta_j)+\nu_{ij},\ i,j\in\{1,\ldots,N\} \qquad (7)$$

where the quantity $\nu_{ij}=\nu_{ij}^{(R)}+i\nu_{ij}^{(I)}$ represents the complex-valued measurement noise and potential modeling errors. In the remainder, we assume that measurement noise is only due to the finite integration time in the above expression and all other sources of error are properly eliminated by adequate modeling and by calibration. Consequently, $\nu_{ij}^{(R)}$ and $\nu_{ij}^{(I)}$ become independent and identically distributed (i.i.d.) zero-mean Gaussian random variables with variance σ_ν^2 for $i=j$ and variance $\sigma_\nu^2/2$ for $i\neq j$ and σ_ν^2 depends inversely on the duration of the time-averaging, that is, the integration time. Thus, longer integration times result in smaller noise variance. Measurements of mutual intensity can be expressed in the matrix form $\boldsymbol{\Gamma}=[\Gamma_{ij}],i,j\in\{1,\ldots,N\}$ which is the Hermitian time correlation matrix for the observed EM fields of thermal origin. The diagonal elements of $\boldsymbol{\Gamma}$ are intensity terms proportional to the power received by each antenna. These intensity terms are the subject of microwave thermography. For the sake of discussion, we initially assume that M independent measurements are made for each Γ_{ij} element. It will become apparent later on that a single measurement with a long integration time equal to the sum of those of M independent measurements is also sufficient.

In order to detect change in permittivity or temperature, we define the differential in the mutual-intensity matrix as $\Delta\boldsymbol{\Gamma}=\boldsymbol{\Gamma}-\boldsymbol{\Gamma}_{\text{REF}}$ where $\boldsymbol{\Gamma}_{\text{REF}}$ is the *reference* time correlation matrix for the object before the occurrence of change. In the following, we assume for simplicity that the variance in $\boldsymbol{\Gamma}_{\text{REF}}$ is much smaller than σ_ν^2. The real and imaginary parts of the differential mutual-intensity measurements (elements of $\Delta\boldsymbol{\Gamma}$) are collected in a column vector denoted by $\boldsymbol{\varkappa}$, obtained by lexicographic ordering of the upper triangles (including the diagonal) of $\mathcal{R}e\{\Delta\boldsymbol{\Gamma}\}$ and $\mathcal{I}m\{\Delta\boldsymbol{\Gamma}\}$. In this manner, the real-valued vector $\boldsymbol{\varkappa}$ represents a data point in $K=N^2$ dimensional space. In contrast, the diagonal intensity terms lie in a smaller N dimensional space. In the absence of anomaly, the components of $\boldsymbol{\varkappa}$ are Gaussian random variables with zero mean and covariance $\boldsymbol{\Lambda}$ i.e. $\boldsymbol{\varkappa}\sim\mathcal{N}(0,\boldsymbol{\Lambda})$. Here, the covariance matrix $\boldsymbol{\Lambda}$ is diagonal, indicating the independence of the observations, and one has $[\boldsymbol{\Lambda}]_{ii}=\sigma_\nu^2$ when the corresponding element of $\boldsymbol{\varkappa}$ is a diagonal (intensity) element of $\Delta\boldsymbol{\Gamma}$ and $[\boldsymbol{\Lambda}]_{ij}=\sigma_\nu^2/2$ when the corresponding element of $\boldsymbol{\varkappa}$ is an off-diagonal element of $\Delta\boldsymbol{\Gamma}$. In the presence of an anomaly, $\boldsymbol{\varkappa}$ is distributed as $\mathcal{N}(\boldsymbol{\kappa},\boldsymbol{\Lambda})$ with non-zero and unknown mean $\boldsymbol{\kappa}$ which depends on the nature of the anomaly. The detection problem can now be cast into a binary hypothesis testing problem where the null hypothesis $\mathcal{H}_0:\boldsymbol{\kappa}=0$ corresponds to the absence of anomaly and the alternative hypothesis $\mathcal{H}_1:\boldsymbol{\kappa}\neq 0$ corresponds to the

presence of an anomaly. The GLRT can be applied to detect the presence of anomaly with unknown mean vector $\boldsymbol{\kappa}$ using the natural logarithm of the generalized likelihood ratio $L(\boldsymbol{x}) = \ln(f_{\boldsymbol{x}}(\boldsymbol{x}|\mathcal{H}_0)) - \ln(f_{\boldsymbol{x}}(\boldsymbol{x}|\check{\boldsymbol{x}},\mathcal{H}_1))$. Here, $f_{\boldsymbol{x}}(\boldsymbol{x}|\mathcal{H}_0)$ and $f_{\boldsymbol{x}}(\boldsymbol{x}|\check{\boldsymbol{x}},\mathcal{H}_1)$ are the probability density functions (pdf) of the random vector $\boldsymbol{x}$ under the null hypothesis and under the alternative hypothesis, respectively. These pdfs are given by

$$f_{\boldsymbol{x}}(\boldsymbol{x}|\mathcal{H}_0) = ((2\pi)^M|\boldsymbol{\Lambda}|)^{-1/2} \exp\left\{\frac{1}{2}\sum_{m=1}^{M}\boldsymbol{x}_m^T\boldsymbol{\Lambda}\boldsymbol{x}_m\right\} \text{ and}$$

$$f_{\boldsymbol{x}}(\boldsymbol{x}|\check{\boldsymbol{x}},\mathcal{H}_1) = \left((2\pi)^M|\boldsymbol{\Lambda}|\right)^{-1/2} \exp\left\{\frac{1}{2}\sum_{m=1}^{M}(\boldsymbol{x}_m-\check{\boldsymbol{x}})^T\boldsymbol{\Lambda}(\boldsymbol{x}_m-\check{\boldsymbol{x}})\right\}$$

where

$$\check{\boldsymbol{x}} = \frac{1}{\boldsymbol{M}}\sum_{\boldsymbol{m}=1}^{\boldsymbol{M}}\boldsymbol{x}_m$$

is the maximum likelihood estimate of the unknown mean vector $\boldsymbol{\kappa}$ and $|\boldsymbol{\Lambda}|$ is the determinant of $\boldsymbol{\Lambda}$. The explicit expression for the generalized log-likelihood ratio is

$$L(\boldsymbol{x}) = \frac{M}{2}\check{\boldsymbol{x}}^T\boldsymbol{\Lambda}\check{\boldsymbol{x}} = \frac{1}{2}\sum_{k=1}^{K}z_k^2 \tag{8}$$

where $z_k = \sqrt{M}\check{\boldsymbol{x}}_k/\sigma_k$ and σ_k^{-1} is the k'th diagonal element of $\boldsymbol{\Lambda}$. The decision rule for the GLRT is

$$L(\boldsymbol{x}) \begin{array}{c} \text{choose}\,\mathcal{H}_1 \\ > \\ < \\ \text{choose}\,\mathcal{H}_0 \end{array} \gamma \tag{9}$$

where γ is the decision threshold. Note that under $\mathcal{H}_0$ one has $z_k \sim \mathcal{N}(0,1)$ and under $\mathcal{H}_1$ one has $z_k \sim \mathcal{N}(\bar{z}_k,1)$ where the mean $\bar{z}_k = \sqrt{M}\kappa_k/\sigma_k$. Furthermore, since $\check{\boldsymbol{x}}$ is the only statistic (derived from the differential mutual-intensity data) needed for decision making, $\check{\boldsymbol{x}}$ is a *sufficient statistic*. Now, let $f_L(\ell|\mathcal{H}_i)$ denote the pdf of $L(\boldsymbol{x})$ under the hypothesis $\mathcal{H}_i$ for $i \in \{0,1\}$, then $f_L(\ell|\mathcal{H}_0)$ is a chi-square distribution with K degrees of freedom. On the other hand, under $\mathcal{H}_1$ one has $f_L(\ell|\mathcal{H}_1) = \int_{\Omega} f_L(\ell|\lambda,\mathcal{H}_1)d\lambda$ where $f_L(\ell|\lambda,\mathcal{H}_1)$ is a non-central chi-square distribution with K degrees of freedom and non-centrality parameter $\lambda = \sum_{k=1}^{K}\bar{z}_k$ and Ω is the set of all possible values of λ. With the knowledge of $f_L(\ell|\mathcal{H}_i)$ for $i \in \{0,1\}$, one can determine the probability of false alarm for threshold γ as

$$P_{FA}(\gamma) = P(L \geq \gamma|\mathcal{H}_0) = 1 - \int_{-\infty}^{\gamma} f_L(\ell|\mathcal{H}_0)d\ell \tag{10}$$

Similarly, the probability of detection for threshold γ is obtained as

$$P_D(\gamma) = P(L \geq \gamma|\mathcal{H}_1) = 1 - \int_{-\infty}^{\gamma} f_L(\ell|\mathcal{H}_1)d\ell \tag{11}$$

Because the non-centrality parameter λ depends on the unknown nature of the anomaly, the conditional pdf $f_L(\ell|\lambda,\mathcal{H}_1)$ and the ensuant pdf $f_L(\ell|\mathcal{H}_1)$ in (11) are not known a priori. However, with proper sampling of the anomaly and computation of the resulting mutual intensities, one can approximate $f_L(\ell|\mathcal{H}_1)$ as

$$f_L(\ell|\mathcal{H}_1) \approx \sum_{n=1}^{N_s} P(\boldsymbol{h}_n) f_L(\ell|\lambda(\boldsymbol{h}_n),\mathcal{H}_1) \tag{12}$$

where N_s is the sample size, that is, the number of cases with anomaly, $\boldsymbol{h}_n$ is a vector of parameters describing the anomaly (e.g. permittivity, temperature, size, position etc.) for the n'th sample, and $P(\boldsymbol{h}_n)$ is the probability of occurrence of the sample described by $\boldsymbol{h}_n$. Note in the above that the dependence of the non-centrality parameter on the anomaly is made explicit by the notation $\lambda(\boldsymbol{h}_n)$. The probabilities given by (10) and (11) can be used to assess the potential of CMR in conjunction with GLRT (CMR–GLRT) to detect permittivity and temperature change in objects. Examples will be investigated in the next section using Monte-Carlo simulations.

Noise in the estimate $\check{\boldsymbol{x}}$ of the unknown mean vector $\boldsymbol{\kappa}$ is the primary factor determining the error performance of CMR–GLRT. In order to quantify the error performance, we note that the components $\check{\boldsymbol{x}}_k$ $(k \in (1,\ldots,K))$ of $\check{\boldsymbol{x}}$ are sums of M i.i.d. Gaussian random variables. Consequently, they are also Gaussian random variables with variance $\sigma_M^2 = \sigma_v^2/M$ if the component corresponds to a diagonal element of $\Delta\boldsymbol{\Gamma}$ and with variance $\sigma_M^2/2$ if it corresponds to an off-diagonal element of $\Delta\boldsymbol{\Gamma}$. As a result, the standard deviation σ_M is recognized as the normalization factor of the means $\bar{z}_k$. In MW radiometry, measurement noise due to finite integration time is described by the radiometric resolution, that is, sensitivity, which is the minimum temperature difference ΔT detectable by the radiometer. The noise standard deviation σ_M is proportional to ΔT and without loss of generality we can assume the relation $\sigma_M = \Delta T$. For an ideal Dickie radiometer, one has $\sigma_M = \Delta T = 2T_{SYS}/\sqrt{B\tau}$ where T_{SYS} is the thermal noise temperature of the radiometer system and τ is the integration time of the radiometer. Furthermore, $T_{SYS} = T_{ANT} + T_{REC}$ where T_{ANT} is the equivalent noise temperature collected by the antenna and T_{REC} is the equivalent noise temperature of the receiver. For fixed noise bandwidth and system temperature, it is clear that σ_M decreases with increasing τ. The relation $\sigma_M = \sigma_v/M$ then implies that a single measurement with a long integration time $\tau = M\tau'$ (τ' is the integration time of each of the M independent measurements) yields the same noise performance as the collective performance

of M independent measurements. Another important noise specification parameter is the SNR, defined for radiometers as $SNR = T_{ANT} / \Delta T$ which can be related to system parameters as $SNR = 0.5\sqrt{B\tau}\, T_{ANT} / T_{SYS}$ for an ideal Dickie radiometer.

Strictly speaking, the above noise expressions are valid for total power radiometer systems, and some of the actual expressions for noise in correlation radiometers are slightly more complicated [8]. Nonetheless, to first-order, they can be used as estimates of the noise performance for coherent radiometer systems.

III. NUMERICAL SIMULATIONS

In this section, results of Monte-Carlo simulations are discussed to demonstrate the feasibility of CMR–GLRT for the non-imaging detection of permittivity/temperature change. As one potential application domain, we simulate the detection of tumors in breast cancer diagnosis that has been the subject of significant research over the last 40 years. The basic measurement geometry is given in Fig. 1, where the breast is modeled as a hemisphere. The diameter of the hemispherical model is 100 mm and is assumed to consist of a homogeneous internal region of fatty tissue enclosed by an outer skin layer with 2 mm thickness. The mean temperature of the breast tissue is assumed to be 307 K [16] for women between 30 and 45 years of age and the malignant tumor is assumed to have an increased mean temperature difference of +2 K from the rest of the tissue. These physical parameters, along with the electrical parameters of the breast tissue and the tumor taken from [17], are given in Table I. A malignant tumor is modeled as a spherical inclusion in the fatty region. Three diameters for the inclusions, namely 5 mm, 7.5 mm, and 10 mm are considered, each representing a different pathological case. To further simplify analysis, it is assumed that the tumors are located along the z–axis at a discrete set of points separated by 5 mm between the depths 10 mm–40 mm measured from the base of the hemisphere. Tumor diameter and location parameters along with permittivity (Table I) and temperature, constitute the parameter vector $\boldsymbol{h}_n$ for each tumor. In total, there are $N_s = 21$ different cases representing a 'random' sample from the population of all pathological cases.

A Monte-Carlo realization consists of computation of the internal fields of the breast model at 3.5 GHz for a set of plane waves incident from several directions and the subsequent computation of the set of all mutual intensities. In this study, incidence directions (θ,ϕ), are restricted to the xz–plane, constituting the set $\theta \in \{n\pi/12\}$ where $n = \{0,\ldots,5\}$ and $\phi \in \{-\pi,\pi\}$. Noting that the directions $(0,-\pi)$ and $(0,\pi)$ are identical, there are $N = 11$ incidence i.e. observation directions. In addition, both parallel polarization and perpendicular polarization defined with respect to the plane of incidence i.e. the xz–plane, are considered. The mutual intensity $\Gamma_p^{(N)}(\boldsymbol{\psi}_1,\boldsymbol{\psi}_2)$ for both polarizations are computed using (4) for each pair of incidence (observation) directions resulting in $K = 121$-dimensional data space for each polarization. In total, $2K$ mutual intensities (both polarizations) are computed for the tumor-free breast model comprising a set of reference measurements and $2K$ mutual intensities are computed for each pathological case.

TABLE I. PHYSICAL PARAMETERS OF BREAST TISSUE AND TUMOR

	Skin	Fatty Tissue	Tumor
Relative Permittivity	36.0	9.0	50.0
Conductivity (S/m)	4.0	0.4	4.0
Layer Thickness (mm)	2.0	48.0	-
Mean Temperature (K)	307.0	307.0	309.0

The fields inside the breast model are computed for plane wave incidence by Finite Difference Time Domain (FTDT) using the commercial CST software. The FTDT domain is a 120 mm × 120 mm × 70 mm box where the z–axis is aligned with the short edge of the box spanning from z = –10 mm to z = 60 mm. The base of the hemisphere is aligned with the xy–plane of the FTDT domain and the center of the base is selected as the origin of the coordinate system. Finally, the size of the Yee cell for the FTDT simulations is 2 mm × 2 mm × 2 mm, corresponding to the volume Δv in (4).

The 11-by-11 reference mutual-intensity matrix $\boldsymbol{\Gamma}_{\text{REF}}$ (i.e. for tumor-free breast model), computed by FTDT EM field simulations is shown in Figs. 2 and 3 for parallel and perpendicular polarizations, respectively. In both figures, the real part of the matrix is on the left side and the imaginary part of the matrix is on the right side of the figure. The matrix elements are the true mutual-intensity values containing no measurement noise. The real and imaginary parts of the matrix are symmetric and anti-symmetric, respectively, due to the conjugate symmetry property of mutual intensity, that is, $\Gamma_p(\boldsymbol{\psi}_1,\boldsymbol{\psi}_2) = \Gamma_p^*(\boldsymbol{\psi}_2,\boldsymbol{\psi}_1)$. The main diagonal of the matrix corresponds to the intensities observed in each direction having the highest (brightest) values in the real part and zero imaginary part. The darker blue strips along the upper and lower diagonals (more apparent in Fig. 2) indicate that there is considerable negative correlation between EM fields in directions separated by angles in the range 45°–60°. Note also that the real and imaginary parts are also symmetric and anti-symmetric respectively, with respect to the main skew-diagonal. This implies that the mutual intensity of EM fields in any pair of directions are conjugated when the directions pair is rotated about the z–axis by 180°. This is a result of the azimuthal symmetry in the breast model. Although the mutual-intensity matrix patterns for the two polarizations look similar, the dynamic ranges of the real and imaginary parts are larger at parallel polarization compared to perpendicular polarization. It is also interesting that the imaginary part at perpendicular polarization is about an order of magnitude smaller than its real part.

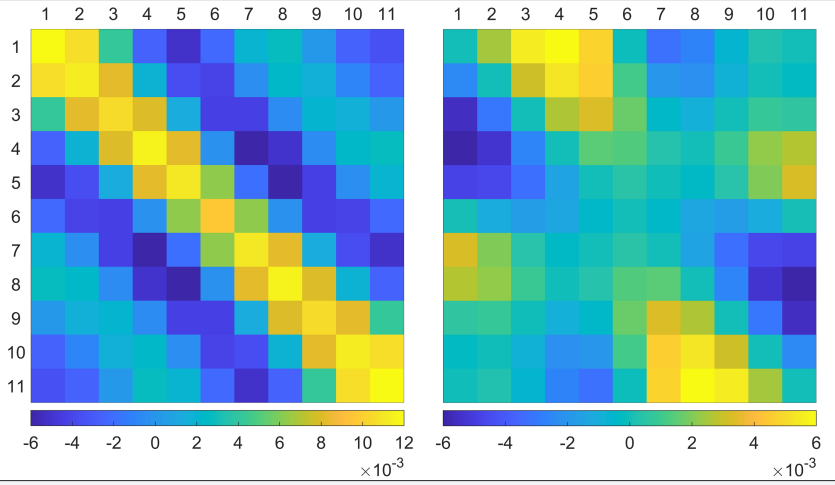

Fig. 2. Reference mutual-intensity matrix Γ_{REF} for parallel polarization (left) real part, (right) imaginary part.

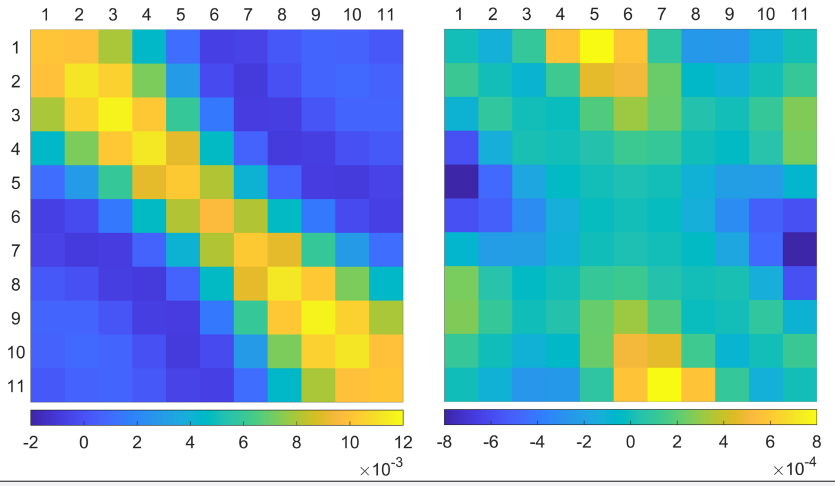

Fig. 3. Reference mutual-intensity matrix Γ_{REF} for perpendicular polarization (left) real part, (right) imaginary part.

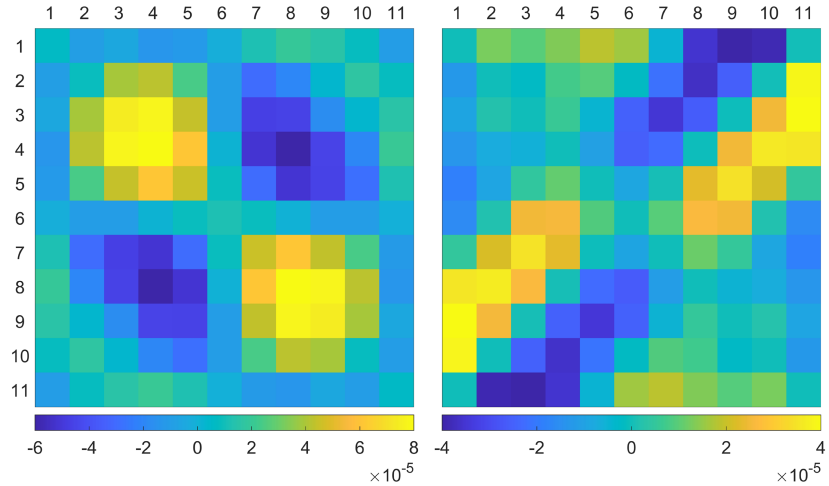

Fig. 4. Differential mutual-intensity matrix $\Delta\Gamma$ for parallel polarization (left) real part, (right) imaginary part.

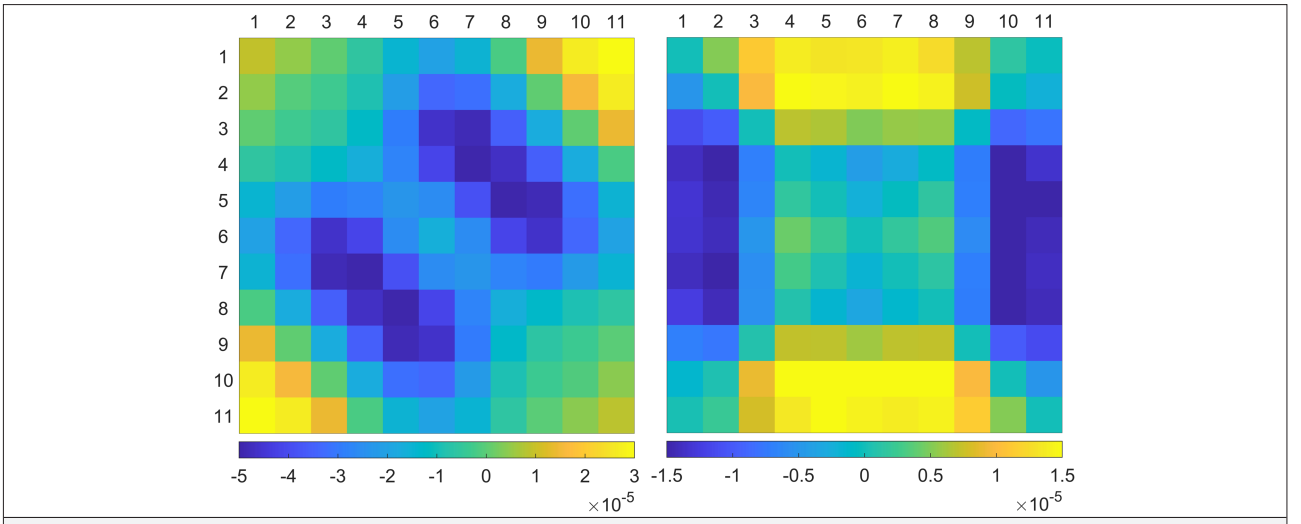

Fig. 5. Differential mutual-intensity matrix $\Delta\mathbf{\Gamma}$ for perpendicular polarization (left) real part, (right) imaginary part.

The differential intensity matrices $\Delta\mathbf{\Gamma}$ (without noise) for the inclusion with 10 mm diameter and located at $z = 30$ mm from the base of the hemisphere, are depicted in Figs. 4 and 5 for parallel and perpendicular polarizations, respectively. As before, the real and imaginary parts of the matrix are on the left and right images of both figures, respectively. Here, the brightest values do not necessarily reside on the main diagonal of the real part, but the remaining properties of the mutual-intensity matrix are inherent. Note that there are clear patterns apparent in the matrix. These patterns are different for the two polarizations and also change with inclusion size and location, suggesting that these patterns can be exploited for detection of inclusions. Note that the differential mutual-intensity values are, on average, about two orders of magnitude smaller (−20 dB) than the mutual-intensity values. Also, the dynamic ranges in real and imaginary parts at perpendicular polarization are lower compared to parallel polarization. The differences in patterns will lead to different detection performances for the two polarizations.

For measurements with noise, radiometer system parameters need to be specified to determine measurement noise. We assume $T_{ANT} = T_{REC} = 307\ K$, the average breast tissue temperature, yielding $T_{SYS} = 614$ K. The bandwidth is chosen as $B = 100$ MHz which yields $\sigma_M = \Delta T \approx 0.12\tau^{-1/2}$ K and $SNR \approx 34 + 5\log(\tau)$ dB. The means $\bar{z}_k (k \in \{1,\ldots,121\})$ and subsequently the corresponding non-centrality parameters λ are obtained from the measured differential mutual intensities (i.e. with noise) for each of the 21 cases and for both polarizations. The pdf $f_L(\ell|\mathcal{H}_1)$ is then computed using equation (12) with $P(\boldsymbol{h}_n) = 1/N_s$ where N_s is sample size in a specific scenario. The equal probability assumption is reasonable under the lack of prior information on the probabilities of size and location of the tumors.

In order to provide more insight, the pdfs $f_L(\ell|\mathcal{H}_0)$ and $f_L(\ell|\mathcal{H}_1)$ are plotted in Fig. 6, for the 5 mm-diameter inclusion with $\tau = 25$ ms and parallel polarization. Here, $N_s = 7$ because only the inclusion location is variable in this scenario. This τ value yields a $SNR = 26$ dB and $\sigma_M = \Delta T = 0.78K$. The gross overlap of the pdfs in the figure suggests that the detection performance will be low for this inclusion with this integration time. In contrast, the pdfs depicted in Fig. 7 for the 10 mm-diameter inclusion with $\tau = 25$ ms and parallel polarization,

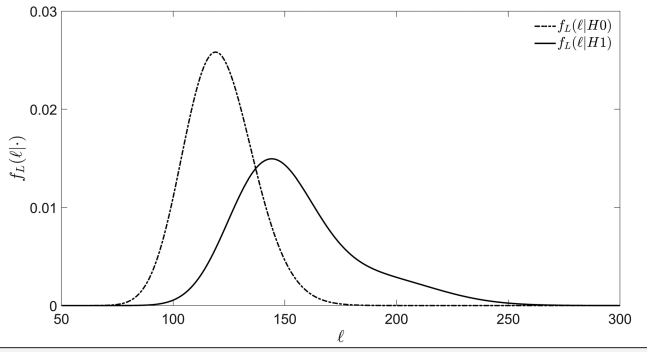

Fig. 6. Log-likelihood pdfs for 5 mm-diameter inclusion for $\tau = 25$ ms and parallel polarization.

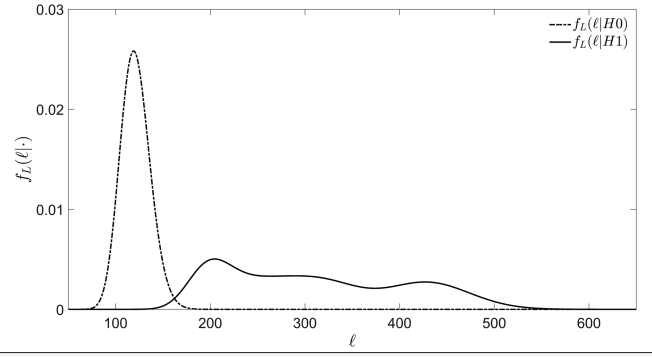

Fig. 7. Log-likelihood pdfs for 10 mm-diameter inclusion for τ = 25 ms and parallel polarization.

have very little overlap. Consequently, much better detection performance can be expected for the latter inclusion.

For better assessment of detection performance, Receiver Operator Characteristics (ROC) curves for the CMR–GLRT are plotted in Fig. 8 corresponding to the 5 mm-diameter inclusion for parallel polarization and $\tau = 50$ ms, resulting in a $SNR = 27.5$ dB and $\Delta T = 0.55$ K. The solid curve in the figure corresponds to the ROC with mutual-intensity data and the dashed curve corresponds to the ROC with intensity-only data i.e. the diagonal elements of $\Delta\mathbf{\Gamma}$. The large difference between the mutual intensity and intensity-only ROC curves is a result of the fact that mutual-intensity data are much larger ($K = 121$) than the intensity data which consist of only 11 intensity measurements. Consequently, the former results in larger λ values driving $f_L(\ell|\mathcal{H}_1)$ further away from $f_L(\ell|\mathcal{H}_0)$. This is a general result implying that the performance of MW thermography can be greatly improved by using coherent radiometry at the cost of increased hardware complexity, calibration and processing.

The effect of polarization on performance is illustrated in Fig. 9, where ROCs for the two polarizations are compared for the 5 mm-diameter inclusion. In the figure, there are two pairs of ROC curves and in each pair, parallel and perpendicular polarizations are represented by the solid and dashed lines, respectively. The pairs are identified by their integration times $\tau = 25$ ms and $\tau = 50$ ms. For both τ values, the performance of parallel polarization is superior compared to perpendicular polarization. This is not a general tendency however. A different outcome, not shown here, is observed for the 7.5 mm-diameter inclusion where the two polarizations have similar performance for long integration times and perpendicular polarization outperforms parallel polarization for short integration times. In the

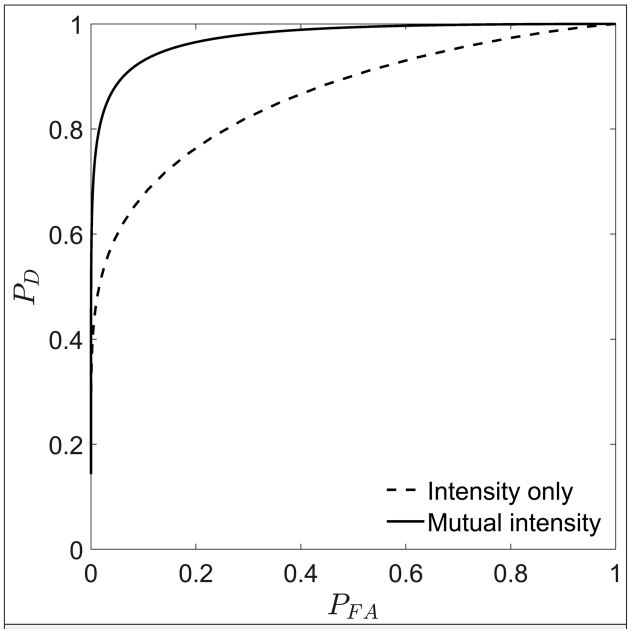

Fig. 8. ROC curves corresponding to 5 mm-diameter inclusion for τ = 50 ms and parallel polarization.

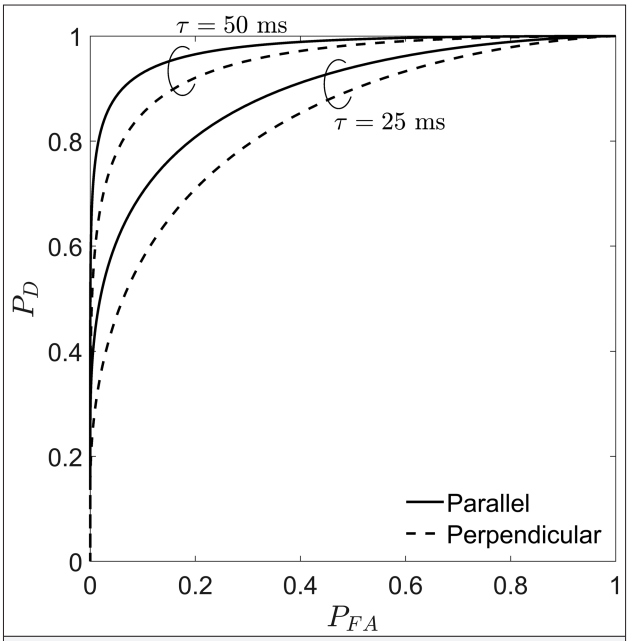

Fig. 9. ROC curves for parallel and perpendicular polarizations corresponding to 5 mm-diameter inclusion.

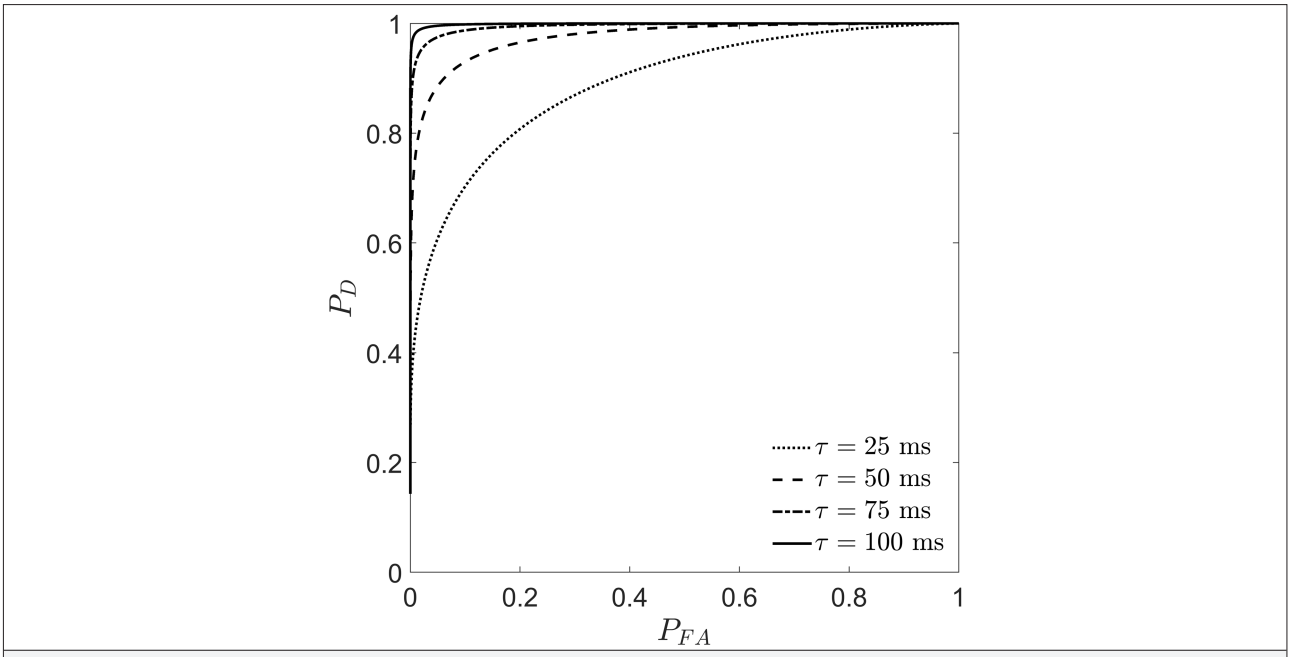

Fig. 10. ROC curves parameterized by integration time τ, for the 5 mm-diameter inclusion and parallel polarization.

remainder of this paper, only results for parallel polarization will be presented.

As previously mentioned, change detection performance of CMR–GLRT depends on measurement noise (ΔT or SNR) which influences the variances of the pdfs in Figs. 6 and 7. Apparently, pdfs with smaller variance will have smaller overlap, yielding better detection performance. For a system with constant T_{SYS} and B as is the case in this study, noise is regulated by the integration time. The effect of integration time is explored in Fig. 10 for the 5 mm-diameter inclusion and parallel polarization. In the figure, the ROC curves are parameterized by τ, assuming values from the set {25,50,75,100} in units of ms. The corresponding values for SNR are 28.4 dB and 29 dB, and the corresponding values for ΔT are 0.45 K and 0.39 K for $\tau = 75$ ms and $\tau = 100$ ms, respectively. As expected, the detection performance improves substantially with increasing τ, and is especially good for $\tau = 100$ ms, even for the smallest inclusion considered here. Also note that the improvement rate is larger at lower values of τ. Similar results are obtained for perpendicular polarization but are omitted here.

The final aspect investigated is the effect of inclusion size on detection performance. In Fig. 11, ROC curves parameterized by the inclusion diameter are plotted for parallel polarization. The integration time for these ROC curves is selected as $\tau = 25$ ms. It is evident from the figure that as the inclusion diameter d increases, detection performance is improved considerably. This behavior is expected as a result of the foregoing discussion on the pdfs $f_L(\ell|\mathcal{H}_0)$ and $f_L(\ell|\mathcal{H}_1)$; the separation of the pdfs grows with particle size (Figs. 6 and 7). In general, the size of the anomaly to be detected is unknown a priori, so in order to accommodate this uncertainty into the ROC, $f_L(\ell|\mathcal{H}_1)$ is computed using inclusions of all three sizes, assuming equal probability of occurrence with $N_s = 21$. The ROC for this combined case is plotted with the dashed line (designated as 'combined') in Fig. 11. The resulting 'average' ROC approximately describes the detection performance for a spherical inclusion of arbitrary diameter between 5 and 10 mm. The average ROC shows a detection performance

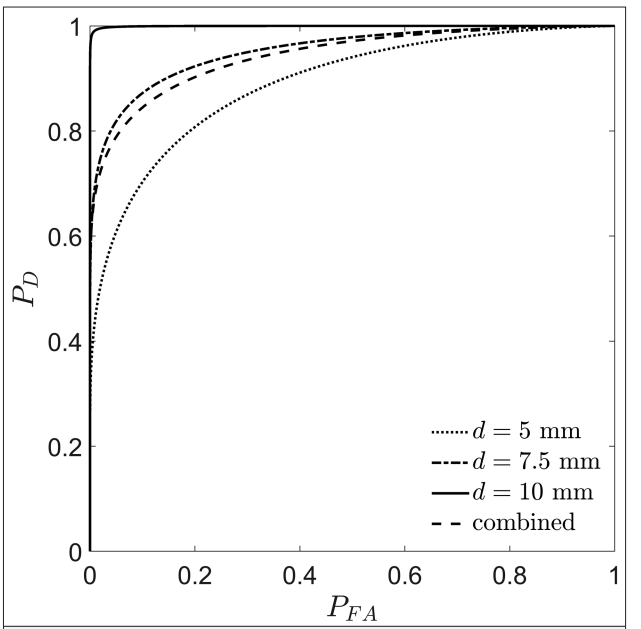

Fig. 11. ROC curves parameterized by inclusion diameter d, for $\tau = 25$ ms and parallel polarization.

superior to the case with d = 5 mm alone but inferior to the cases with larger inclusions.

IV. DISCUSSION

The results of the numerical simulations of the previous section are encouraging. These simulations, however, are performed under rather favorable assumptions and several issues need to be addressed before the proposed CMR–GLRT method can be considered feasible.

One important drawback for radiometric systems is the rather long data acquisition time, that is, integration time, compared to active systems which can be several orders of magnitude shorter with ultra wideband near-field radar imaging systems. As is shown in Fig. 10, an integration time of at least 100 ms is necessary to achieve good performance for detection of small tumors. This integration time also corresponds to the total data acquisition time if all measurements are made simultaneously, requiring a coherent receiver with N = 11 channels. Keeping in mind that the corresponding noise level is $\sigma_M = \Delta T = 0.39K$, this level of sensitivity can be attained with a receiver with a well-designed internal calibration network for coherent noise distribution among channels. These requirements will eventually increase system complexity and cost. Alternatively, it is possible to compute pairwise correlations of the EM fields with only a two-channel coherent receiver and a switch matrix resulting in a much simpler system. The drawback of the latter system is that with N = 11 directions, there are 66 mutual intensities, that is, complex correlations. With τ = 100 ms, this translates to 6.6 s of data acquisition time for each polarization. In medical applications like breast tumor detection, long acquisition times are a disadvantage because of patient movement. The data acquisition time increases as $\mathcal{O}(N^2)$, so the latter design accommodating pairwise measurements may be inconvenient if more correlations are required.

An alternative to increasing integration time is to decrease receiver temperature T_{REC} or increase system bandwidth B. A decrease in T_{REC} by 100 K is possible and will cut integration time by 30%—a modest gain for the same SNR. On the other hand, increasing bandwidth has a more direct effect on integration time, for example, for B = 1 GHz the integration time will be τ = 10 ms for the same SNR. However, wide bandwidths will induce decorrelation of the EM fields. When decorrelation ensues, the off-diagonal elements of $\mathbf{\Gamma}$ tend to zero and $\mathbf{\Gamma}$ converges to a diagonal matrix, reducing CMR to intensity-only thermography, in effect. The relatively low performance of intensity-only systems was demonstrated in Fig. 8. In order to ensure that decorrelation does not ensue, the quasi-monochromatic condition must be satisfied [6], according to which the maximum dimension of the breast model must be much smaller than the correlation length $\ell_c = v/B$ within the breast, where $v \approx 10^8$ m/s is the speed of EM waves inside the breast (fatty tissue only). The correlation lengths within the breast tissue are $\ell_c = 1$ m and $\ell_c = 0.1$ m for bandwidths B = 100 MHz and B = 1 GHz, respectively. Considering that the hemispherical model has a diameter of 0.1 m, the quasi-monochromatic condition is not satisfied for B = 1 GHz, meaning that decorrelation is inevitable. As a result, only a modest increase in bandwidth seems possible. Furthermore, it was tacitly assumed that the electrical parameters of the skin, breast tissue, and tumor were constant within the 100 MHz bandwidth. For larger bandwidths, this assumption may not be valid, in which case the use of a Debye dielectric model will be more appropriate [18].

Another issue is presence of sources other than a local anomaly, that can cause a bias in $\Delta\mathbf{\Gamma}$, resulting in an increased false alarm rate. For example, any mismatch in antenna locations of the reference measurements and those of subsequent measurements will result in a residual differential intensity even in the absence of an anomaly. This should not be an issue in the far-field for small location mismatch. Similarly, changes in object temperature may occur due to changes in the ambient temperature or other activity; for example, the average breast temperature may change due to physiological activity/dysfunction [16]. In this case, the level of uncertainty may be larger than the sensitivity of ΔT = 0.39 K for τ = 100 ms. If the change in temperature is uniform throughout the object, the bias may be eliminated by proper normalization of the mutual-intensity matrix $\mathbf{\Gamma}$ (e.g. normalization by the difference of the maximum and minimum values of the diagonal elements) because mutual intensity is linear in temperature. For non-uniform temperature changes that are not anomaly-induced, other methods like thermal modeling will need to be devised.

V. CONCLUSION

A simple non-imaging CMR–GLRT method is proposed for detection of change in the temperature or the permittivity of a lossy object. The method is based on the GLRT, where the signals to be detected are the complex correlations of the EM fields at pairs of points distributed around the object. Factors affecting performance are discussed by analyzing ROC curves computed using Monte-Carlo simulations, with application to breast cancer diagnosis. The analysis is done with the complex correlations of EM fields in the far-field of the object. This is not a restriction, however, and the method can also be used in the near-field.

The analysis results demonstrate that the differential mutual intensity can be used with CMR–GLRT to detect small tumors (5 mm in diameter, modeled as spherical inclusions) with high detection probability and low probability of false alarm. Assuming that in the absence of anomaly, temperature and permittivity remain constant over time, the ROC of the method is directly influenced by the radiometric resolution of the correlation radiometer. There is significant improvement in the ROC when mutual-intensity data are used as opposed to the use of intensity-only data.

The current study can be regarded as an initial analysis step before more detailed imaging analysis of an object is made.

There are several challenges associated with the proposed method, including decreasing acquisition times, which are long-compared to active systems and the possibility of change in the temperature of the object without the development of a local anomaly, like a tumor. The latter change will be detected but will not be distinguished from a local anomaly, leading to increased false-alarm rate. In conclusion, with sufficient improvement, the CMR technique may be used effectively as a prescreening system.

Notwithstanding the promising numerical simulation results, the proposed technique for non-destructive detection of temperature and/or permittivity change is short of experimental verification. The authors are working towards implementing a functioning prototype of a correlation radiometer in order to test the proposed technique. Finally, it is anticipated that with proper modification GLRT may be applied with CMR data at pixel/voxel level, similar to the active imaging studies in [12–15], for the development of a CMR-based qualitative imaging technique.

Peer Review: Externally peer-reviewed.

Author Contributions: Concept – C.U.; Design – C.U.; Supervision – C.U.; Data Collection and/or Processing – C.U., O.A.; Analysis and/or Interpretation – C.U., O.A.; Literature Search – C.U.; Writing Manuscript – C.U.; Critical Review – C.U., O.A.

Conflict of Interest: The authors have no conflicts of interest to declare.

Financial Disclosure: The authors declared that this study has received no financial support.

REFERENCES

1. S. Kwon and S. Lee, "Recent advances in microwave imaging for breast cancer detection," *Int. J. Biomed. Imaging*, vol. 2016, no. 5054912, 2016. [CrossRef]
2. R. C. Conceicao, J. J. Mohr and M. O'Halloran, Eds., *An Introduction to Microwave Imaging for Breast Cancer Detection*. Cham, Switzerland: Springer, 2016.
3. R. Benny, T. A. Anjit and P. Mythili, "An overview of microwave imaging for breast tumor detection," *Prog. Electromagn. Res. B*, vol. 87, 2020, pp. 61–91. [CrossRef]
4. K. L. Carr, "Microwave radiometry: Its importance to the detection of cancer," *IEEE Trans. Microw. Theor. Tech.*, vol. 37, no. 12, pp. 1862–1869, 1989. [CrossRef]
5. S. Vesnin, A. K. Turnbull, J. M.Dixon and I. Goryanin, "Modern microwave thermometry for breast cancer," *J. Mol. Imaging Dynam.*, vol. 7, no. 2, 2017. [CrossRef]
6. C. Utku, "Microwave coherence imaging: A novel electromagnetic imaging technique," *IEEE Trans. Geosci. Remote Sens.*, pp. 1–16, 2020. [CrossRef]
7. A. R. Thompson, J. M. Moran and G. W. Swenson, Jr., *Interferometry and Synthesis in Radio Astronomy*. Cham, Switzerland: Springer, 2017.
8. C. S. Ruf, C. T. Swift, A. B. Tanner and D. M. Le Vine, "Interferometric synthetic aperture microwave radiometry for the remote sensing of the Earth," *IEEE Trans. Geosci. Remote Sens.*, vol. 26, no. 5, pp. 597–611, 1988. [CrossRef]
9. Y. Leroy, B. Bocquet and A. Mamouni, "Non-invasive microwave radiometry thermometry," *Physiol. Meas.*, vol. 19, no. 2, pp. 127–148, 1998. [CrossRef]
10. S. M. Kay, *Fundamentals of Statistical Signal Processing: Detection Theory*. Upper Saddle River, NJ: Prentice-Hall, 1998.
11. C. M. Trott, R. B. Wayth, J.-P. R. Macquart and S. J. Tingay, "Source detection in interferometric visibility data: I. Fundamental estimation limits," *Astrophys. J.*, vol. 731, no. 2, pp. 81–94, 2011. [CrossRef]
12. H. Brunzell, "Clutter reduction and object detection in surface penetrating radar," *Proc. Radar*, vol. 97. Edinburgh, UK: IEEE, 1997, pp. 688–691.
13. S. K. Davis, H. Tandradinata, S. C. Hagness and B. D. Van Veen, "Ultrawideband microwave breast cancer detection: A detection-theoretic approach using the generalized likelihood ratio test," *IEEE Trans. Bio. Med. Eng.*, vol. 52, no. 7, pp. 1237–1250, 2005. [CrossRef]
14. G. Shi and A. Nehorai, "A relationship between time-reversal imaging and maximum-likelihood scattering estimation," *IEEE Trans. Signal Process.*, vol. 55, no. 9, pp. 4707–4711, 2007. [CrossRef]
15. D. Ciuonzo, "On time-reversal imaging by statistical testing," *IEEE Signal Process. Lett.*, vol. 24, no. 7, pp. 1024–1028, 2017. [CrossRef]
16. A. Lubkowska and M. Chudecka, "Thermal characteristics of breast surface temperature in healthy women," *Int. J. Environ. Res. Public Health*, vol. 18, no. 3, p. 1097, 2021. [CrossRef]
17. Y. Xie, B. Guo, L. Xu, J. Li and P. Stoica, "Multistatic adaptive microwave imaging for early breast cancer detection," *IEEE Trans. Biomed. Eng.*, vol. 53, no. 8, 2002, pp. 1647–1657. [CrossRef]
18. X. Li and S. C. Hagness, "A confocal microwave imaging algorithm for breast cancer detection," *IEEE Microw. Wirel. Comp. Lett.*, vol. 11, pp. 130–132, 2001.

Cüneyt Utku received his B.Sc. and M.Sc. in electronics and communication engineering from the Istanbul Technical University and his Ph.D. degree in electrical engineering from the George Washington University in 2007. He worked at the Hydrospheric and Biospheric Sciences Laboratory of NASA Goddard Space Flight Center as a research fellow of the NASA Postdoctoral Program and later of the Goddard Earth Sciences Technology and Research Program, working at the Cryospheric Sciences Laboratory, NASA Goddard Space Flight Center, Greenbelt, Maryland. He worked at the Istanbul Sehir University, Istanbul, Turkey and is currently with the Informatics and Information Security Research Center of the Scientific and Technological Research Council of Turkey (TUBITAK), Kocaeli, Turkey.

Onur Arı received B.Sc. degree in the Department of Electronics and Communication Engineering from Suleyman Demirel University, Turkey in 2011. Also, he received his M.Sc. degree in the same department of Suleyman Demirel University, in 2013. He is currently pursuing Ph.D. degree in the department of electronics and communication engineering at Yildiz Technical University, Turkey. He is a senior researcher in the department of sensor and antenna systems, the Informatics and Information Security Research Center of the Scientific and Technological Research Council of Turkey (TUBITAK), Kocaeli, Turkey.